Supplementary information

Supplementary Video 1. Simulations show that distinct chromocenters exist for a finite amount of time in models with only lamina attraction but no chromocenter pinning.

Supplementary Video 2. Chromocenters fuse over time in simulations of nuclear inversion.

Supplementary Figure 1. Sorting and identification of rod perikarya. Microscopic control of cells used for Hi-C.

Supplementary Figure 2. Highly expressed genes are not specifically associated with nuclear pores in rod cells.

Supplementary Figure 3. Repositioning of rhodopsin gene from the nuclear interior to the nuclear periphery in the course of nuclear inversion in differentiating rods

Supplementary Figure 4. Quantitative comparison of simulations to microscopy is robust to choice of metric.

Supplementary Figure 5. Rescue of the conventional nuclear architecture in de-differentiated rods of R7E retina

Supplementary Figure 6. Our model is robust to perturbations and outperforms a variety of other models.

Supplementary Table 1. Hi-C Read and Filtering Statistics

Supplementary Table 2. List of BACs used in this study.

Supplementary Information 1. Energies for Polymer Simulations

Supplementary References

Supplementary Video 1. Simulations show that distinct chromocenters exist for a finite amount of time in models with only lamina attraction but no chromocenter pinning.

Beginning simulations from initial configurations generated at optimal point (iii) in Fig 3d, we released chromocenter pinning from the lamina, while maintaining all monomer-monomer interactions. While we removed C-lamina pinning, we kept C-lamina and B-lamina attractions, which had equal magnitude. We then visualized 10 simulations replicates (columns), showing three simultaneous great circle sections from each (rows). Even without chromocenter pinning, distinct chromocenters persisted for a finite amount of time before eventually merging.

Supplementary Video 2. Chromocenters fuse over time in simulations of nuclear inversion.

Beginning simulations from initial configurations generated at optimal point (iii) in Fig 3d, we removed interactions of monomers with the lamina, while maintaining all monomer-monomer interactions. We then visualized 10 simulations replicates (columns), showing three simultaneous great circle sections from each (rows). Chromocenters moved away from the lamina and merged as spherical droplets until they finally coalesced into a large central chromocenter.

Supplementary Figure 1. Microscopic control of cells used for Hi-C

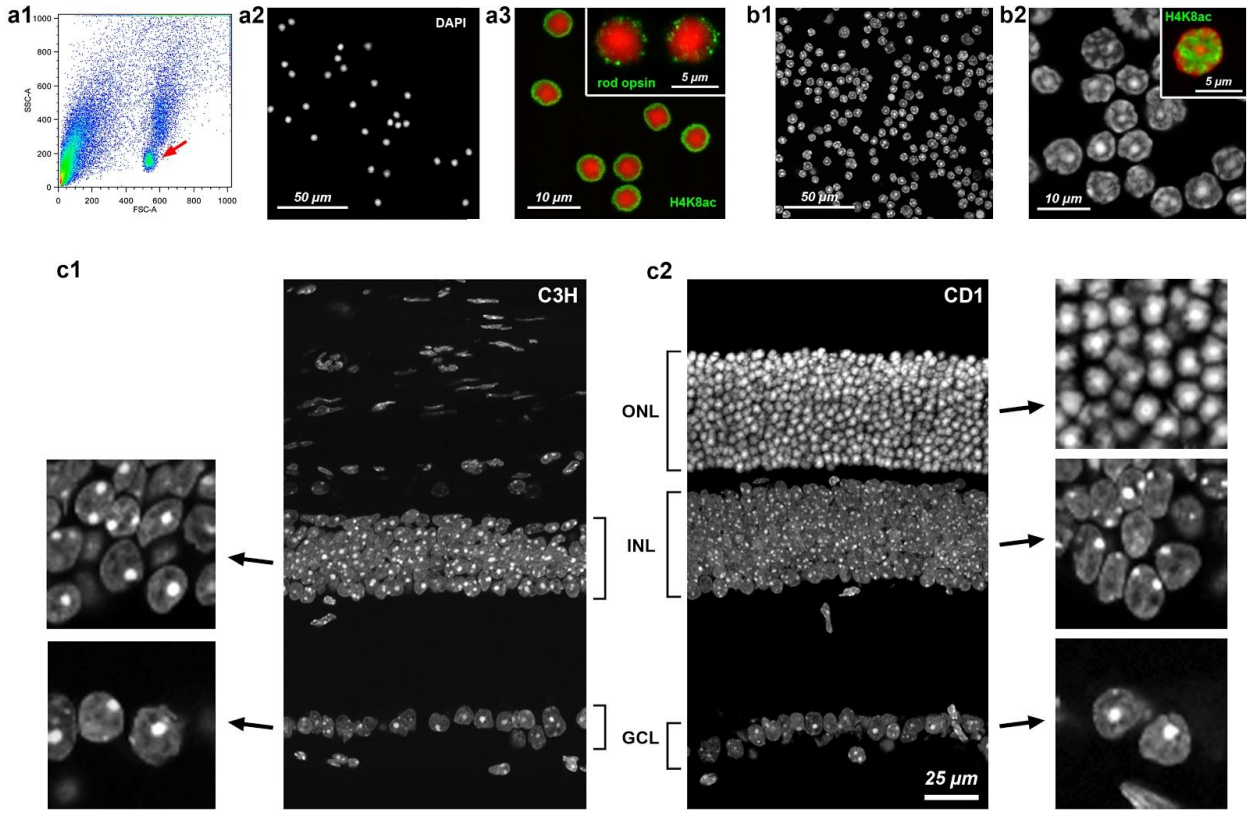

a, sorting and identification of rod perikarya. FAC sorting of retina suspensions based on standard forward and sideward scatter settings yields a distinct population of rod cells (**a1**, *red arrow*). The purity of the rod perikarya population can be estimated after DAPI staining (**a2**). Rod cell identity is confirmed by euchromatin (H4K8ac) staining (**a3***, green*) revealing inverted nuclear structure and anti-rhodopsin staining (*insertion in* **a3***, green*); nuclei are counterstained with DAPI (*red*).

b1,2, suspension of WT thymocytes obtained by dissociation of CD1 mouse thymus; DAPI staining. Euchromatin staining (**b2**, *insertion*) reveals conventional nuclear organization in these cells.

c1, cryosection of a C3H mouse retina used for obtaining non-rod neurons. Retinas of adult C3H mice are lacking the entire Outer Nuclear Layer (ONL). Close-ups of the other two nuclear layers, Inner Nuclear Layer (INL) and Ganglion Cell Layer (GCL) are shown on the left. For comparison, **c2** shows retina of CD1 mice consisting of three layers; close-ups of all three layers, including ONL consisting mostly of rods, are on the right.

Images are single confocal sections.

Supplementary Figure 2. Both expressed and silenced genes localize to the euchromatic peripheral shell in rod nuclei but are not specifically associated with nuclear pores.

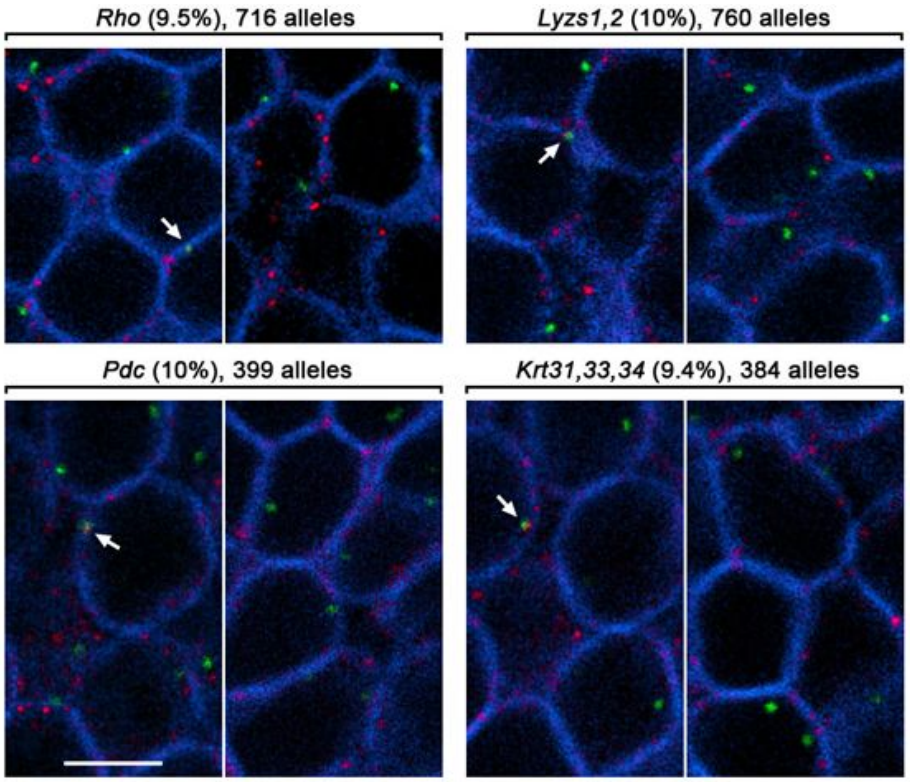

The genic part of the mouse genome, regardless of its transcriptional activity, is adjacent to the nuclear lamina of rods and constitutes an euchromatic peripheral shell. To prove whether occasional proximity of genes to nuclear pores correlates with gene expression, two FISH experiments were performed.

Active and inactive loci were detected in the same nuclei pair-wise: expressed rhodopsin *(Rho)* and silenced lysozymes 1,2 *(Lyzs1,2);* expressed phosducin *(Pdc)* and silenced hair keratin gene cluster *(Krt31,33,34).* All four gene loci are peripheral in rod nuclei with about 10% being proximal to nuclear pores (*arrows*). Expressed and silenced genes have equal frequency of microscopically detected association with the pores as indicated in brackets above the panels. Only overlapping signals were considered as being associated (*arrows*). Numbers of scored alleles are indicated above the panels. FISH signals are *green,* immunostained nuclear pores are *red*, immunostained lamina (lamin B1) is *blue*. Single confocal sections; scale bar, 5 μm. BACs used for gene detection: *Rho*, RP23-357N10; *Pdc*, RP23-53N22; *Lyzs1,2*, RP23-326O5; *Krt31,33,34*, RP24-86N10. Antibodies: mouse-anti-Nup153 (Abcam, ab24700) and goat-anti-LamB1 (Santa Cruz, sc-6217). The experiment was repeated three times.

Supplementary Figure 3. Repositioning of rhodopsin gene from the nuclear interior to the nuclear periphery in the course of rod nuclear inversion during postnatal development of retina

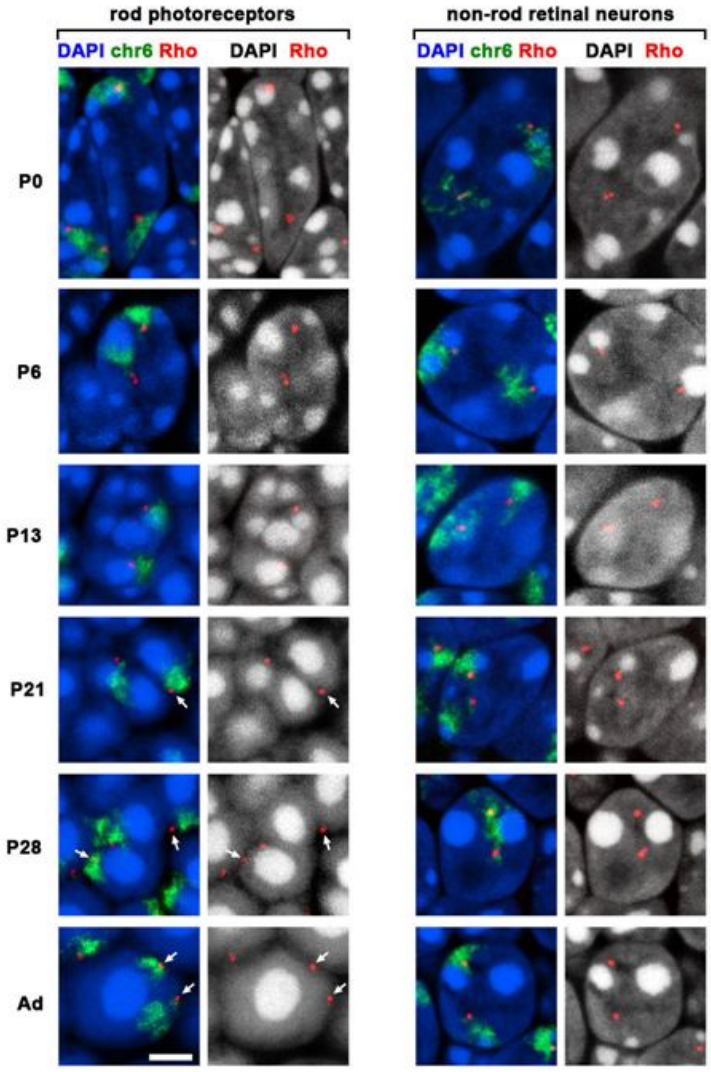

Differentiation of rod photoreceptors is accompanied by a drastic reorganization of rod nuclear architecture from conventional to inverted. Importantly, in the course of inversion, the rhodopsin gene (*Rho, red*) situated within a relatively gene-rich locus on chromosome 6 (*green*) moves together with euchromatin and thus changes its position from internal to peripheral (*two left columns*). Note, that in some cells, the *Rho* gene reaches the nuclear periphery already at P21-P28 and remains peripheral in adults (*arrows*). In contrast, in other retinal neurons, the *Rho* gene remains in the nuclear interior during the entire retina development (*two right columns*). Scale bar, 2 μm and applies to all panels. Projections of 1-2 μm confocal stacks. Probes, FISH and microscopy are described in the *Methods*. The experiment was repeated twice.

Supplementary Figure 4. Quantitative comparison of simulations to microscopy is robust to choice of metric.

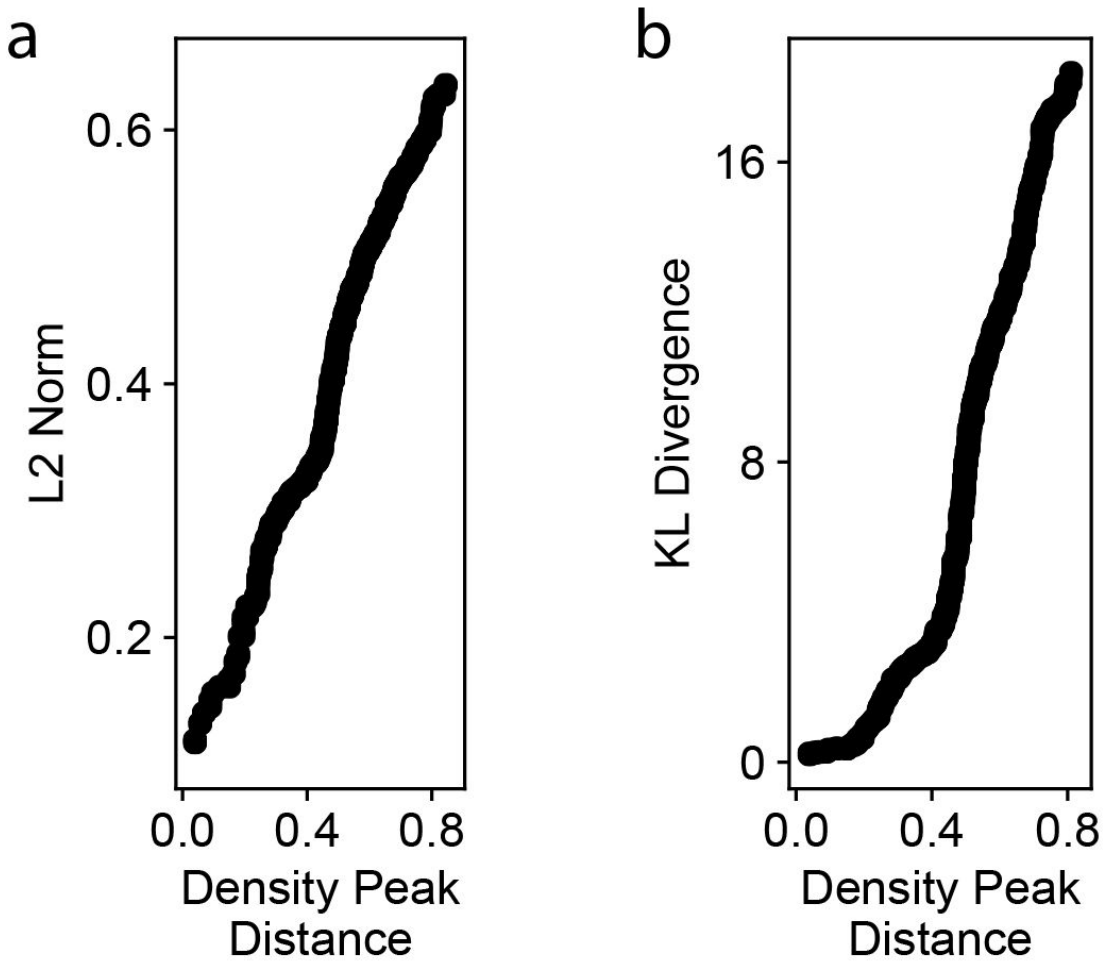

Comparing the density peak distance used in the text to measure agreement of simulation data to microscopy to other measures of probability distribution distance shows that our results are not sensitive to the choice of metric. In particular, for each of the 720 model classes discussed in Fig. 2b, we compute the L^2 norm (**a**) and the Kullback-Leibler Divergence (**b**) of the simulated density functions (see Methods). For both alternative metrics, we find that the alternative metric and the density peak distance are in an almost one-to-one, monotonically increasing relationship (Spearman's r=.99 for both).

Supplementary Figure 5. Rescue of the conventional nuclear architecture in de-differentiated rods of R7E retina

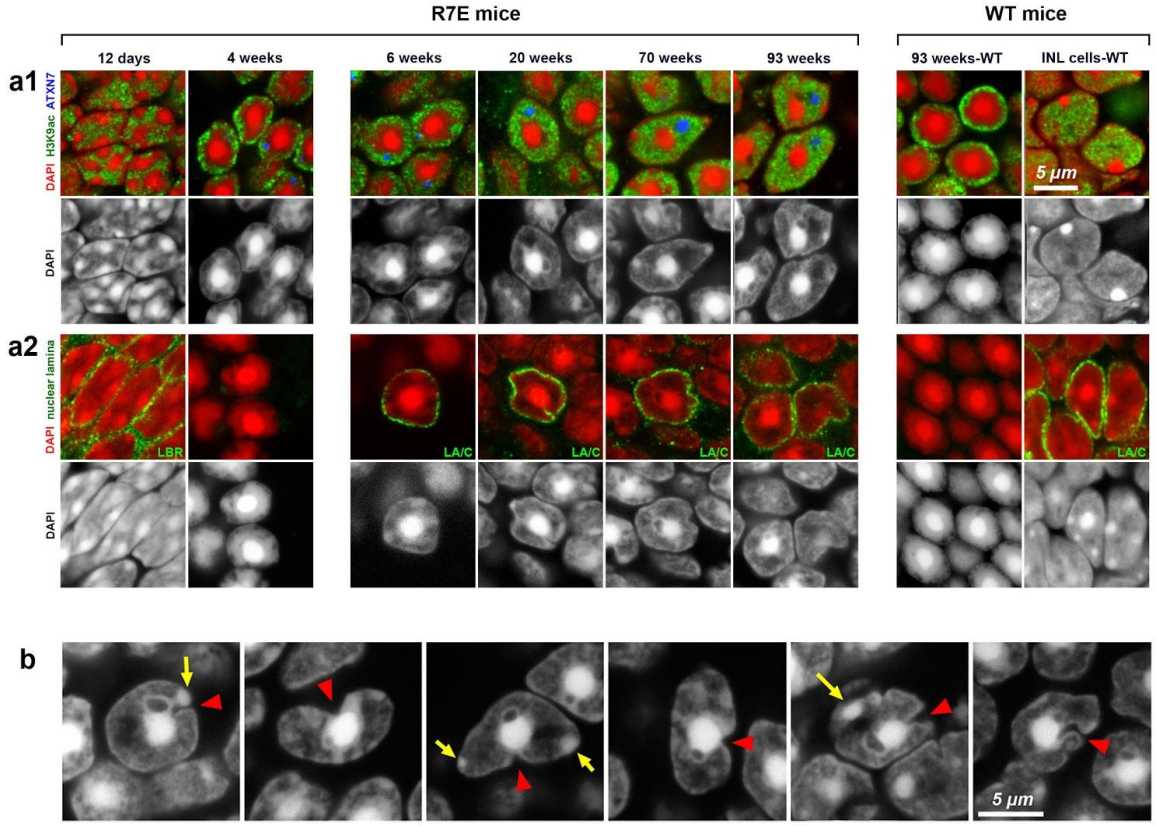

In the mouse model for spinocerebral ataxia type 7, R7E, retinal cells heterozygously express human polyQ-expanded ataxin-7 (ATXN7) and remain seemingly normal until the age of 3-4 weeks (**a**, *left column*; compare to WT rod nuclei in the *right column*). After this developmental point, ATXN7 becomes concentrated in a single nuclear inclusion (**a1**, *blue granules*) and the entire retina begins to degenerate. The accumulation of expanded ATXN7 is accompanied by decreased expression of the master regulators of cell differentiation in photoreceptors in general (*Crx*) and in rods in particular (*Nrl* and *Nr2e3*). As a consequence of the massive downregulation of rod-specific genes, rod cells lose their identity and undergo strong morphological changes such as degradation of the outer segments, shortening of axons and widening of the perikarya cytoplasmic layer[1] (*mid column*).

Rod de-differentiation is accompanied by gradual changes of the rod nuclear architecture leading to nuclear de-inversion (**a,** *mid column***, b**). First, euchromatin of the peripheral shell leaves the periphery and relocates to the nuclear interior (**a1**, *green*). Second, lamin A/C expression is initiated (**a2**, *green*) and the shell of LINE-rich heterochromatin around the chromocenter dissociates, establishing a broad contact with the nuclear lamina (**a,** *mid column***)**. The large single chromocenter of rods remains bulky in de-differentiated rods, although splitting of individual chromocenters (1-3) can be observed in about half of the cells (**b**, *yellow arrows*). Remarkably, lamina still establishes contacts with such chromocenters by forming invaginations towards them (**b**, *red arrowheads*).

Immunostaining of retinal cryosections using antibodies for euchromatin H3K9ac (**a**, *green*), ATXN7 (**a**, *blue*), LBR and lamin A/C (**b,** *green*). Single optical sections. Immunostaining experiments were repeated three times.

Supplementary Figure 6. The proposed model is robust to perturbations and outperforms a variety of alternative models.

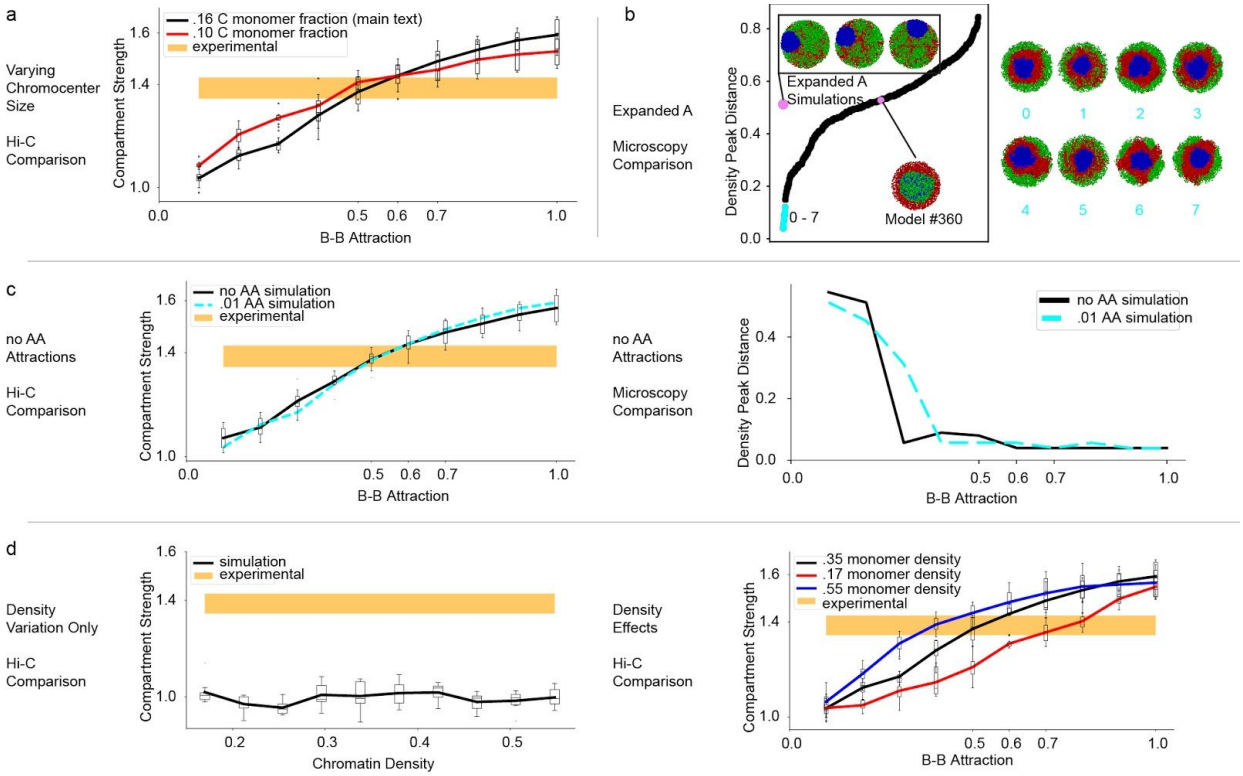

a, Changing C monomer chromosome fraction flattens the curve of compartment strength versus B-B attraction, but does not qualitatively change its behavior. Best-fits for compartment strength remain close to B-B attraction value of 0.5. Boxes: lines indicate median obtained in simulations (n=8 simulated chromosomes), whiskers extending to 1.5 times interquartile range. Orange region shows agreement with Hi-C in rods (+/- one s.d. from median).

b, We compare simulated configurations of a model with expanded A regions to microscopy data (big pink dot), and find it does not perform nearly as well as best-performing models with attractions (models 0-7, cyan). It is quantitatively as far away from the experimental data as model 360 (small pink dot). Densities computed from 50 simulated configurations.

c, Compartment strength does not change quantitatively between no A-A attraction simulations and small A-A attraction simulations. (*right*) Agreement to microscopy shifts only slightly, agreeing well with microscopy beginning at .3 kT B-B attraction for our no A-A simulations, as opposed to .4 kT for our small A-A simulations. (*left*) The range of B-B which is optimal according to Hi-C is also optimal according to microscopy, for both models. For the left figure, quantities plotted as in (a). For the right figure, lines indicate median compartment strengths (n=50, the number of time points sampled across 3 simulation replicates)

d, (*left*) Changing the density of the model, with no special interactions between monomers, does not result in a compartment strength comparable to experiment. (*right*) Changing simulation density in the presence of B-B attractions shifts the curve of compartment strength versus B-B attraction, but does not qualitatively change its behavior. Quantities plotted as in (a). (n=8 simulated chromosomes)

Supplementary Table 1. Hi-C Read and Filtering Statistics

Cell Type and Replica Number		Total Reads	Reads After Filtering	Cis Reads >10kb
Rods	R1	156,913,060	18,030,234	5,105,041
	R2	152,605,824	25,944,021	6,349,206
Non-rod Neurons	R1	116,252,619	19,226,557	5,650,359
	R2	146,003,208	40,646,198	15,748,047
LBR-null Thymocytes	R1	156,172,508	51,945,401	23,387,464
	R2	142,846,173	44,963,418	18,715,738
WT Thymocytes	R1	144,508,673	44,190,905	28,022,538
	R2	151,520,833	50,278,218	31,134,393

Primary Tissue Hi-C for Comparison[2]

Cell Type and Replica Number	Total Reads	Reads After Filtering	Cis Reads >10kb
Bladder, R1	233,041,838	52,456,550	24,121,444
Bladder, R2	236,250,557	43,395,294	19,659,511
Adrenal Gland, R1	181,680,303	48,951,415	22,449,886
Psoas Muscle, R1	196,863,028	36,856,215	13,566,008
Psoas Muscle, R2	95,110,351	25,776,091	10,410,829
Pancreas, R1	160,416,883	49,627,891	21,200,091
Pancreas, R2	12,147,138	3,538,979	1,367,214
Pancreas, R3	128,745,528	15,683,831	7,787,867
Lung, R1	308,335,703	85,597,004	24,417,652
Hippocampus, R1	187,658,680	64,151,770	29,220,961

Right Ventricle, R1	672,319,838	179,219,920	63,091,486
Small Bowel, R1	177,864,628	58,017,249	21,073,296
Spleen, R1	378,529,216	107,599,392	33,032,593
Ovary, R1	201,215,217	70,283,904	20,909,766
Dorsolateral Prefrontal Cortex, R1	165,728,687	52,713,868	25,426,433

Supplementary Table 2. List of BACs used in this study.

chromo-some	BAC #	compart-ment (in rods)	full BAC name	BAC coordinates according to GRCm38/mm9 assembly

BACs for tracing chromosomal loci and chromatin compaction estimation during differentiation retinal cell

chr 1	1	B	RP23-301J4	chr1:148,427,249-148,630,696
	2	B	RP24-218I23	chr1:149,531,820-149,662,189
	3	B	RP24-287C18	chr1:150,513,860-150,698,942
	4	B	RP23-149H6	chr1:150,812,163-151,003,321
	5	weak A	RP23-215H3	chr1:151,664,650-151,861,157
	6	A	RP24-318A10	chr1:152,971,124-153,121,132
	7	A	RP23-184H2	chr1:153,525,078-153,731,791
	8	A	RP23-20L20	chr1:154,487,105-154,694,524
chr 2	9	A	RP24-134B13	chr2:93,736,040-93,907,764
	10	A	RP23-214A16	chr2:94,088,207-94,276,965
	11	B	RP23-421B15	chr2:97,663,720-97,847,295
	12	weak B	RP23-340I3	chr2:101,017,004-101,218,085
	13	A	RP24-367D17	chr2:101,903,896-102,048,200
chr 6	14	---	RP23-120L10	chr6:3,025,850-3,271,476
	15	---	RP23-20F16	chr6:3,414,712-3,614,619
	16	A	RP23-317H22	chr6:3,856,716-4,085,483
	17	A	RP23-288L22	chr6:4,525,064-4,696,692

BACs for labeling constitutive A and B compartment loci of chromosome 11

chr 11	18	B	RP23-57E21	chr11:14,107,822-14,360,877
	19	B	RP23-33F12	chr11:25,104,302-25,315,399
	20	B	RP23-263I7	chr11:47,527,023-47,730,951
	21	A	RP23-399H5	chr11:78,274,464-78,467,177
	22	A	RP24-73A8	chr11:97,942,676-98,185,208
	23	A	RP23-82I5	chr11:120,199,525-120,428,921

BACs for labeling *Rho* locus

chr 6	24	A	RP23-116F20	chr6:113,263,811-113,485,267
	25	A	RP23-111F16	chr6:114,002,262-114,189,099
	26	A	RP23-86F18	chr6:114,901,511-115,120,641
	27	A	RP23-219M6	chr6:115,737,278-115,942,756
	28	weak B	RP23-62L5	chr6:116,810,598-116,936,147

Supplementary Information 1. Energies for Polymer Simulations

1. Stretching energy between adjacent monomers along a polymer, of the form $.5k * (r-1)^2$, where r is the distance between adjacent monomers, and k is chosen such that the average deviation $\sqrt{\langle r^2 \rangle}$ of the bond length from its equilibrium of 1 is .05.

2. Harmonic bending energy between adjacent pairs of monomers, of the form $.5 * (1 - cos(\theta))$, where θ is angle between adjacent pairs.

3. Spherical confinement to the nucleus of all polymers, of the form $10 * ({r_0}^2 + (r - r_0)^2)^{\frac{1}{2}}$ if $r > r_0$ and 0 if not. r_0 is chosen such that the density of monomers within the nucleus is .35 [3].

4. For B monomers, attraction to the nuclear lamina of the form $BLam * (L - R + 1) * (R - L + 1)$, where $L = \sqrt{r^2 + .01^2}$, R is the radius of the confining sphere, $BLam$ is an energy drop in units of kT, and -1 < $R - L$ < 1. Outside of this range, the energy is zero.

5. For C monomers, pinning to the lamina was implemented via the same potential for spherical confinement, again with the density of monomers set to .33. The difference here is that the center of the confining sphere is a point on the nuclear lamina, chosen randomly for each polymer's C monomers.

6. For attraction between monomers, we used a potential with a repulsive energy of 5kT when particles are overlapping. This smoothly transitions to a potential well of depth epsilon, which varies depending on the monomer types involved in the interaction. The attractive part finally goes to zero at $r = 1.8$, so the potential well does not extend further than one other monomer. The repulsive part is given by:

   $5 * (1 + r_{rep}^{12}(r_{rep}^2 - 1) * (\frac{7}{6})^6 7)$, where $r_{rep} = r * \sqrt{\frac{6}{7}}$

   The attractive part is given by:

   $-\epsilon * (1 + r_{att}^{12}(r_{att}^2 - 1) * (\frac{7}{6})^6 7)$, where $r_{att} = \frac{(r-1.4)}{.4} * \sqrt{\frac{6}{7}}$

   We additionally include step functions such that the attractive part does not extended below $r = 1$, and such that the repulsive part does not extend above. Each monomer type is assigned a "stickiness" value, and ϵ is then the geometric mean of the stickinesses of the two monomers involved in the interaction, in units of kT.

Supplementary References:

1. Helmlinger, D. *et al.* Glutamine-expanded ataxin-7 alters TFTC/STAGA recruitment and chromatin structure leading to photoreceptor dysfunction. *PLoS Biol.* **4**, e67 (2006).
2. Schmitt, A. D. *et al.* A Compendium of Chromatin Contact Maps Reveals Spatially Active Regions in the Human Genome. *Cell Rep.* **17**, 2042–2059 (2016).
3. Ou, H. D. *et al.* ChromEMT: Visualizing 3D chromatin structure and compaction in interphase and mitotic cells. *Science* **357**, (2017).